Journal of Alloys and Compounds 1068 (2026) 188545

Contents lists available at ScienceDirect

Journal of Alloys and Compounds

journal homepage: www.elsevier.com/locate/jalcom

Zeolite-assisted synthesis of electrocatalysts with atomically dispersed Fe sites for high-efficiency ORR

Zheyan Tang [a], Hongwei Zhao [a,*], Meiyu Chen [a], Lixiang Li [a,*], Siqi Guan [a], Lin Wu [a], Huaiyang Zuo [a], Han Zhang [a], Jingang Zheng [a], Lin Tao [a], Chengguo Sun [a,b], Qingdong Li [c], Xueyuan Zhang [c], Baigang An [a,c,**]

[a] Key Laboratory of Energy Materials and Electrochemistry Research Liaoning Province, School of Chemical Engineering, University of Science and Technology Liaoning, Anshan 114051, China
[b] School of Chemical Engineering, Nanjing University of Science and Technology, Nanjing 210094, China
[c] Institute of Corrosion Science and Technology, Guangzhou 510530, China

ARTICLE INFO

Keywords:
Zeolite
Chemical vapour deposition
Open porous structure
Electrocatalyst
Oxygen reduction reaction

ABSTRACT

Developing high-performance and cost-effective electrocatalysts for oxygen reduction reaction (ORR) is pivotal to advancing sustainable energy conversion technologies such as fuel cells and metal–air batteries. However, conventional pyrolysis methods for synthesizing iron and nitrogen co-doped porous carbon (Fe-N-C) electrocatalysts often suffer from carbon framework shrinkage at high temperatures. This leads to pore narrowing or collapse, severely restricting active-site exposure and hindering mass transport. This study presents a zeolite-assisted synthesis of Fe–N/NC electrocatalysts with abundant Fe–N_x sites and stable, open porous structures using Fe-ion-exchanged zeolite (FeY-zeolite), direct chemical vapour deposition (CVD) of acetonitrile vapour and acid etching. During CVD, the Fe species within the FeY-zeolite promote the formation of highly active Fe–N_x sites. The rigid zeolite framework enables the retention of abundant open micro-/mesoporous structures within the electrocatalysts through reverse replication during acid etching. The optimised Fe–N/NC-900 electrocatalyst exhibits a high specific surface area of 1815 $m^2\ g^{-1}$, a well-defined open porous structure, atomically dispersed Fe sites, and abundant Fe–N_x active centres. This results in outstanding ORR activity in alkaline electrolytes, with a high half-wave potential of 0.83 V, a large limiting current density of 6.1 mA cm^{-2} comparable to that of a 20% Pt/C electrocatalyst, and a high current retention rate of up to 95.6%. Theoretical calculations confirm that the Fe–N_x sites facilitate the desorption of OH* intermediates, thereby promoting ORR. This work highlights the potential of the zeolite-assisted strategy to synergistically optimise mass transport and electrocatalytic activity, offering a viable route for designing high-performance non-precious-metal ORR electrocatalysts.

1. Introduction

Oxygen reduction reaction (ORR) is a critical process in emerging energy storage and conversion systems such as fuel cells and metal–air batteries [1,2]. However, ORR requires highly efficient electrocatalysts to overcome its sluggish reaction kinetics. Although commercial Pt/C electrocatalysts are amongst the most effective in ORR [3–5], the high cost and scarcity of Pt resources hinder large-scale applications. Consequently, high-performance non-precious-metal electrocatalysts, such as metal- and nitrogen-co-doped carbon (M–N–C, M = Fe, Co, Ni, etc.), are attracting increasing attention [6–9]. Amongst these, Fe–N–C electrocatalysts have demonstrated outstanding ORR performance, excellent conductivity, and the ability to activate O_2 molecules [10,11]. On the Fe–N_x sites, the single dz^2 electron of Fe^{2+} can readily penetrate the antibonding π orbital of O_2, facilitating the transfer of electrons from the electrode surface to O_2 molecules and efficiently catalysing ORR [12–14]. In addition, the Fe–N_x sites can modulate the intermediates at various stages of ORR, thereby mitigating undesirable side reactions such as peroxide formation [15]. Moreover, the N atoms in the electrocatalyst can accelerate ORR by altering the charge distribution of

* Corresponding authors.
** Corresponding author at: Key Laboratory of Energy Materials and Electrochemistry Research Liaoning Province, School of Chemical Engineering, University of Science and Technology Liaoning, Anshan 114051, China.
E-mail addresses: hongwei0068@ustl.edu.cn (H. Zhao), lxli2005@126.com (L. Li), bgan@ustl.edu.cn (B. An).

https://doi.org/10.1016/j.jallcom.2026.188545
Received 9 March 2026; Received in revised form 15 April 2026; Accepted 8 May 2026
Available online 10 May 2026

adjacent C atoms and forming active sites for adsorbing and dissociating O_2 molecules [16,17].

Fe–N–C electrocatalysts are primarily prepared via the pyrolysis of precursors containing Fe, N and C elements, during which Fe atoms coordinate with N atoms to create Fe–N_x active sites in an N-doped porous carbon framework [18–20]. As the porous nature can markedly increase the utilisation of electrocatalysts and favour O_2 transport, developing Fe–N–C electrocatalysts with a micro-/mesoporous structure has emerged as an effective strategy [21–23]. The template-assisted method is an effective approach for constructing hierarchical porous structures for high-performance Fe–N–C electrocatalysts. For example, Han et al. used ordered mesoporous silica (KIT-6), $FeSO_4{\cdot}7\ H_2O$ and 1, 10-phenanthroline monohydrate as templates and precursors to synthesise an Fe–N–C/N-OMC electrocatalyst with remarkable ORR activity, in which the Fe–N_x sites were embedded in a three-dimensional (3D) N-doped mesoporous carbon framework with an ordered porous structure that facilitated mass and electron transport [24]. Zhu et al. fabricated a highly active Fe–N–HMC electrocatalyst with hierarchical micro-/mesopores using SiO_2 as a template and $FeCl_3$ and a tripolycyanamide-based microporous polymer as precursors. The Fe–N_x active sites, combined with a large specific surface area and hierarchical micro-/mesopores, synergistically enhanced the ORR performance of the Fe–N–HMC electrocatalyst [25]. Similarly, Xu et al. employed a dual template of $ZnCl_2$ and NaCl, along with $FeCl_2$ and 1,10-phenanthroline precursors, to fabricate an Fe–N–C electrocatalyst with a hierarchically porous framework. $ZnCl_2$ was employed to create abundant micropores, and NaCl was used to convert specific micropores into mesopores. This unique pore structure enhanced the availability of Fe–N_x active sites, thereby improving ORR performance [26]. However, micropore closure caused by carbon skeleton contraction and collapse during pyrolysis and template removal still needs to be addressed.

Previously, we used silanised zeolite as a template to construct a carbon based metal-free ORR electrocatalyst with highly accessible microporous structures using a reverse replication strategy [27]. The resulting rigid 3D microporous carbon framework effectively prevented pore collapse and closure. However, the absence of metal active sites limited the electrocatalytic performance. Notably, the intrinsic strong ion exchange capability of the zeolite framework offers a practical pathway for introducing metal active sites [28,29]. Upon Fe ion exchange with zeolite, Fe atoms uniformly coordinate within the zeolite framework structure. When integrated with chemical vapour deposition (CVD) using an N-containing organic vapour, this approach enables the formation of atomically dispersed Fe–N_x active sites within the carbon framework. Meanwhile, the spatial confinement effect of the microporous skeleton can effectively prevent aggregation of Fe–N_x sites and micropore blockage. Furthermore, the 3D interconnected open pore network can enhance mass transport and increase the exposure of active sites, thereby improving overall electrocatalytic performance.

Herein, iron and nitrogen co-doped porous carbon (Fe-N/NC) electrocatalysts were successfully synthesised using Fe-ion-exchanged Y zeolite (FeY-zeolite) as the template and acetonitrile as the carbon-nitrogen precursor via direct CVD. As illustrated in Fig. 1, FeY-zeolite was synthesised using the ion exchange capacity of Y zeolite. FeY-zeolite was subjected to CVD using acetonitrile vapour at various pyrolysis temperatures, followed by acid etching. The resulting Fe–N/NC electrocatalysts inherited the unique open microporous structures of the zeolite through reverse replication. The optimised Fe–N/NC-900 electrocatalyst featured a high specific surface area characterised by atomically dispersed Fe atoms and abundant Fe–N_x active sites uniformly distributed throughout its carbon framework. The Fe–N/NC-900 electrocatalyst exhibited notable ORR activity and stability in alkaline media, with a performance comparable to that of 20% Pt/C. In situ electrochemical impedance spectroscopy (EIS) and distribution of relaxation times (DRT) analysis demonstrated the excellent reaction kinetics and rapid mass transfer capability of Fe–N/NC-900. Theoretical calculations confirmed that the Fe–N_x sites facilitated the desorption of OH* intermediates, thereby enhancing the ORR process.

2. Experimental

2.1. Chemicals and regents

Y zeolite (H-form, SiO_2/Al_2O_3=5.8, Na_2O=3.9 wt%, HSZ-320HOA) obtained from Tosoh Corporation, Japan. Iron nitrate nonahydrate ($Fe(NO_3)_3{\cdot}9\ H_2O$, ≥ 98%), acetonitrile (CH_3CN, ≥ 99.8%), hydrochloric acid (HCl, 5.0 M), hydrofluoric acid (HF, ≥ 40%), potassium hydroxide (KOH, ≥ 99%) purchased from Sinopharm Chemical Reagent Co., Ltd. Nitrogen (N_2, ≥ 99.999%) and oxygen (O_2, ≥ 99.999%) supplied by the Liaoning Guoyi New Material Technology Co., Ltd. The 20% Pt/C catalyst was obtained from Johnson Matthey Co., Ltd. The 5% Nafion solution was obtained from DuPont Co., Ltd. All aqueous solutions are prepared with ultrapure water supplied by an ultrapure water system.

2.2. Synthesis FeY-zeolite

The iron ion exchange process involved using 3.0 g of Y zeolite in 180 mL of 0.1 M $Fe(NO_3)_3$ aqueous solution. The mixed solution was maintained at 60 °C for 3 h under reduced pressure, and the ion exchange treatment was repeated twice. The resulting slurry was filtered, thoroughly washed with distilled water, and then dried for 12 h in a vacuum oven set to 80 °C. The powder was further roasted at 550 °C for 4 h in an air atmosphere and named FeY-zeolite.

2.3. Synthesis of Fe-N/NC catalyst

1.0 g of FeY-zeolite was placed in a ceramic boat inside a quartz reactor (35 mm in diameter) and purged with pure nitrogen gas at room temperature for 30 min. The reactor was heated to specific temperatures

Fig. 1. Schematic diagram for the in situ synthesis of Fe-N/NC samples using FeY-zeolite by acetonitrile vapor CVD.

(700, 800, and 900 °C) under N_2 flow at a rate of 10 °C min^{-1}. Subsequently, the N_2 flow was directed into an acetonitrile bubbler maintained at 80 °C, creating an acetonitrile vapor/N_2 mixture (0.20 vol% acetonitrile vapor in 100 mL min^{-1} N_2) that was introduced into the reactor. The chemical vapor deposition (CVD) of acetonitrile vapor was conducted for 4 h at different temperatures (700, 800, and 900 °C). Afterward, the temperature of the quartz reactor was reduced to room temperature in the N_2 atmosphere. Finally, the sample was washed with a mixed solution of HF (20 wt%, 40 mL) and HCl (0.1 M, 40 mL) at room temperature to remove the zeolite. The resultant Fe-N/NC samples were recorded as Fe-N/NC-700、Fe-N/NC-800, and Fe-N/NC-900. The NC-900 was also prepared with the same synthesis conditions using untreated Y zeolite as a template for comparison.

3. Results and discussion

To verify the effectiveness of acetonitrile CVD in achieving carbon deposition on FeY-zeolite, the colour changes in the samples were observed. As shown in Fig. 2a, digital photographs revealed obvious colour changes. White Y zeolite turned yellow after Fe ion exchange, indicating the success of the ion exchange process. After CVD and acid etching, the sample turned black, confirming the efficiency of acetonitrile CVD in furnishing carbonaceous materials. The samples were morphologically characterised using scanning electron microscopy (SEM). In contrast to the smooth surface of Y zeolite (Fig. S1), small particles were observed on the outer surface of FeY-zeolite (Fig. 2b), which can be attributed to the migration and aggregation of excessive metal elements within the zeolite during the high-temperature treatment [31,32]. The surfaces of Fe–N/NC-700 (Fig. S2a), Fe–N/NC-800 (Fig. S2b) and Fe–N/NC-900 (Fig. 2c) showed a rougher texture than NC-900, which was prepared using Y zeolite as a template (Fig. S3). Compared with pure Y zeolite, FeY-zeolite exhibited substantially enhanced carbon deposition activity due to Fe ion exchange, resulting in a more pronounced wrinkling of the carbon-nitrogen layers in the Fe–N/NC samples. This can be attributed to the chemical inertness of the particle surface and pore walls of pure Y zeolite, which is composed of SiO_2 and Al_2O_3, hindering the deposition of carbonaceous substances. However, the carbon deposition activity in the internal regions of FeY-zeolite can be effectively enhanced under transition metal catalysis [30]. In addition, the amount of nitrogen-carbon deposition increased with rising CVD temperature. Thermogravimetric analysis (TGA) of the samples before acid etching further confirmed this result (Fig. S4). The nitrogen-carbon content in NC/Y-zeolite-900 was only 15.2 wt%, which was considerably lower than that in NC/FeY-zeolite-700 (34.0 wt%),

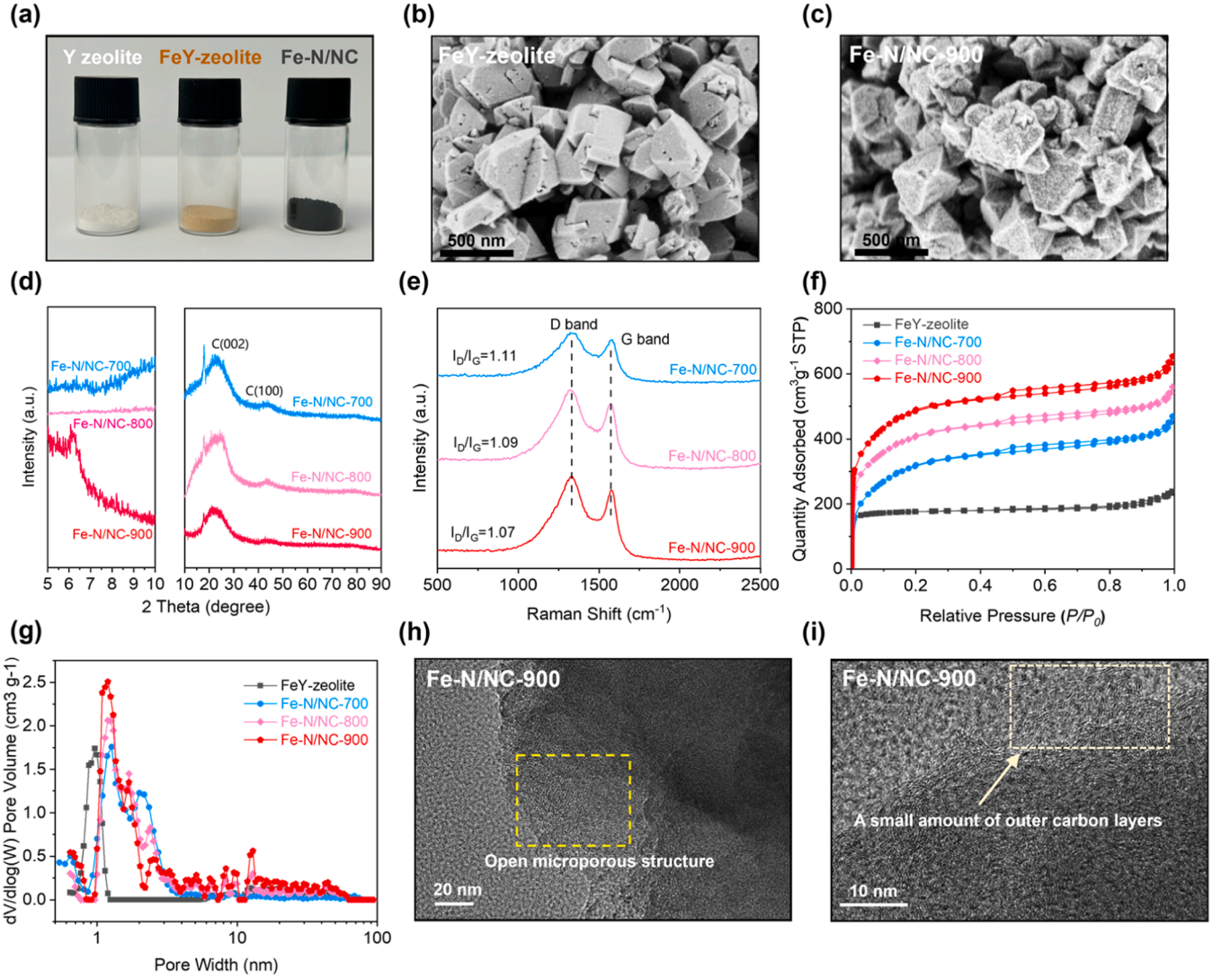

Fig. 2. (a) A digital photograph of Y zeolite, FeY-zeolite, and Fe-N/NC-900. SEM images of (b) FeY-zeolite and (c) Fe-N/NC-900. (d) XRD patterns. (e) Raman spectra. (f) N_2 adsorption–desorption isotherms. (g) Pore size distribution of FeY-zeolite, Fe-N/NC-700, Fe-N/NC-800, and Fe-N/NC-900. (h-i) HRTEM images of the Fe-N/NC-900.

NC/FeY-zeolite-800 (34.2 wt%) and NC/FeY-zeolite-900 (36.1 wt%). The abundant nitrogen-carbon deposition promotes the formation of a stable carbon framework within the zeolite.

In the X-ray diffraction (XRD) patterns (Fig. 2d), only Fe–N/NC-900 showed a distinct diffraction peak in the small-angle region ($2\theta = 6.6^{\circ}$). This diffraction peak is typically attributed to the ordered microporous carbon structure formed via the directional replication of the original ordered microporous zeolite framework [30]. However, the weak intensity of this diffraction peak indicates the presence of an ordered microporous structure in Fe–N/NC-900, but in a relatively low amount. Compared with the other samples, the formation of this ordered microporous structure in Fe–N/NC-900 is attributable to the more abundant nitrogen-carbon deposition, facilitating the partial construction of ordered micropores. In the wide-angle region ($2\theta = 10^{\circ}$–90°), the appearance of two broad peaks at 23° (002) and 44° (100°) can be ascribed to amorphous graphitic carbon [34]. The characteristic peak observed at $2\theta = 17^{\circ}$ may stem from the formation of disordered or turbostratic carbon structures in the samples. These structures increase the interlayer spacing, causing the (002) reflection to shift to a lower angle [35]. Furthermore, the XRD pattern of the Fe–N/NC samples did not exhibit any diffraction peaks associated with the Fe element, indicating the absence of highly crystalline Fe or iron carbides/oxides in the Fe–N/NC electrocatalysts. The defect levels of the prepared materials were assessed using Raman spectroscopy (Fig. 2e), which showed characteristic peaks corresponding to defective sp^3 carbon and graphitic sp^2 carbon at approximately 1350 cm^{-1} (D band) and 1590 cm^{-1} (G band), respectively [33]. The low I_D/I_G ratio of Fe–N/NC-900 (1.07) indicates fewer defects in its graphitic structure compared with Fe–N/NC-700 (1.11) and Fe–N/NC-800 (1.09). The high degree of graphitisation in Fe–N/NC-900 is primarily owing to the relatively high temperature utilised in the CVD process, which facilitates the structural order of carbon.

N_2 adsorption–desorption isotherms were measured for FeY-zeolite, the Fe–N/NC samples and NC-900 at −196 °C (Fig. 2f and Fig. S5a). Unlike FeY-zeolite, which exhibited type-I isotherm characteristics typical of microporous materials [34], Fe–N/NC and NC-900 displayed a hysteresis loop at a medium to high relative pressure ($P/P_0 = 0.5$). All samples exhibited type-IV isotherm characteristics, indicative of their mesoporous structures [36]. In addition, Fe–N/NC-900 exhibited the highest adsorption capacity at $P/P_0 \leq 0.1$ and, in turn, the highest proportion of microporous structure. The pore size distribution curves of FeY-zeolite, the Fe–N/NC samples and NC-900 (Fig. 2g and Fig. S5b) further revealed the evolution of the pore structure. The pore structure of the Fe–N/NC samples predominantly featured micropores in the range of 1–2 nm, considerably differing from the single microporous structure of FeY-zeolite (0.8–1 nm). The TGA and XRD results suggest that the combination of transition metal catalysis and a high CVD temperature promoted carbon deposition within the FeY-zeolite pores, facilitating the construction of a microporous carbon framework with the zeolite microporous structure. Therefore, Fe–N/NC-900 exhibited partially stable, ordered micropores alongside a substantial quantity of disordered micropores, with a micropore content higher than that of other samples. Fe–N/NC-700 and Fe–N/NC-800 contained higher amounts of 2–3 nm mesopores than Fe–N/NC-900, which can be attributed to the relatively poor carbon deposition and low CVD temperature preventing the formation of a stable internal carbon microporous structure. Consequently, during template removal, the micropores tended to collapse and accumulate, transforming into mesopores. Moreover, a high CVD temperature facilitated the conversion of acetonitrile vapour into carbonaceous materials, limiting the deposition of disordered carbon on the external surface of zeolite particles, thereby promoting the formation of mesopores on the external surface. Hence, Fe–N/NC-900 exhibited a higher mesopore content in the 5–20 nm range than the other samples.

Notably, although NC-900 was synthesised under the same high-temperature CVD conditions, the absence of metal sites resulted in no electrocatalytic activity, leading to insufficient carbon deposition and preventing the formation of a stable carbon skeleton. Consequently, the micropore and mesopore contents were considerably lower than those of Fe–N/NC-900, corroborating the crucial role of Fe sites in promoting carbon deposition and the construction of pore structures. As detailed in Table S1, the specific surface area (SSA) and pore parameters of the synthesised samples were systematically evaluated. Benefitting from a highly developed hierarchical micro-/mesoporous architecture, the Fe–N/NC-900 electrocatalyst exhibited the highest overall SSA and micropore surface area (1815 and 1716 $m^2\ g^{-1}$, respectively), considerably outperforming FeY-zeolite (706, 677 $m^2\ g^{-1}$), Fe–N/NC-700 (1157, 996 $m^2\ g^{-1}$), Fe–N/NC-800 (1509, 1407 $m^2\ g^{-1}$) and NC-900 (1154, 1030 $m^2\ g^{-1}$). The high SSA and open micro-/mesoporous structure of Fe-N/NC-900, with a dominant micropore volume of 0.51 $cm^3\ g^{-1}$ and a notable mesopore volume of 0.18 $cm^3\ g^{-1}$, maximises the accessibility of active sites at the triple-phase interface and effectively mitigates O_2 diffusion resistance, thereby enhancing the ORR electrocatalytic activity.

The detailed structural features of Fe–N/NC-900 were observed using high-resolution transmission electron microscopy (HRTEM). The HRTEM image in Fig. 2h shows the open microporous structures of Fe–N/NC-900 as white spots. The rigid pore walls of the zeolite, composed of SiO_2 and Al_2O_3, endow the microporous framework with extremely high thermal stability, preserving the integrity of the framework during the CVD process. This provides favourable conditions for the rapid penetration of the nitrogen-carbon precursor and deposition of the carbon skeleton. Therefore, the carbon skeleton exposed after acid etching remains stable and maintains the open microporous structure. This zeolite-assisted strategy effectively prevents pore collapse and structural contraction commonly observed in conventional high-temperature pyrolysis methods. Fig. 2i illustrates the carbon layer structure on the outer surface of Fe–N/NC-900, revealing that only a limited amount of carbon layers is deposited in a disordered manner under high-temperature conditions. Notably, no nanoparticles or nanoclusters were observed in Fe–N/NC-900. The high SSA of Fe–N/NC-900 contributes to providing a large reaction area, and its open micro-/mesoporous structure facilitates mass transfer and active-site utilisation.

The morphology and distribution of the Fe element in Fe–N/NC-900 were characterised using aberration-corrected high-angle annular dark-field scanning TEM (atomic-resolution HAADF-STEM). As shown in Fig. 3a, numerous distinct bright spots were observed, indicating the presence of abundant atomic-level Fe sites [37]. The HAADF-STEM image (Fig. 3b) and selected area energy-dispersive X-ray spectroscopy (EDX) mapping confirmed the presence of uniformly distributed C, N, O and Fe atoms (Fig. 3c). X-ray photoelectron spectroscopy (XPS) analysis was performed to identify the surface components and chemical states of the samples. The XPS survey spectrum (Fig. 3d) confirmed the presence of C, N and O elements in all Fe–N/NC samples, indicating that N atoms were successfully doped into carbon frameworks via acetonitrile CVD, resulting in the formation of nitrogen-doped carbon layers. The total content of N element (Table S2) in Fe–N/NC-900 (6.52 at%) exceeded that in Fe–N/NC-700 (4.72 at%) and Fe–N/NC-800 (5.69 at%). Although high-temperature pyrolysis typically promotes N loss, elevated temperatures during CVD enhance the deposition of nitrogen-carbon compounds, thereby increasing the content of N-containing functional groups. This observation is consistent with the TGA results. As shown in Figs. 3e and S6, the high-resolution N 1 s spectra of the Fe–N/NC samples can be fitted into five characteristic peaks corresponding to pyridinic-N, Fe–N_x, pyrrolic-N, graphitic-N and oxidised-N at 398.3, 398.9, 399.5, 400.6 and 410.5 eV, respectively [38]. As shown in Table S3, the concentration of active Fe–N_x sites in Fe–N/NC-900 (1.06 at%) was 1.34 and 1.56 times higher than that in Fe–N/NC-700 (0.68 at%) and Fe–N/NC-800 (0.79 at%), respectively. These findings demonstrate that higher CVD temperatures increase nitrogen and carbon deposition, thereby enhancing the formation of additional Fe–N_x sites. Moreover, pyridinic-N and graphitic-N can affect the charge

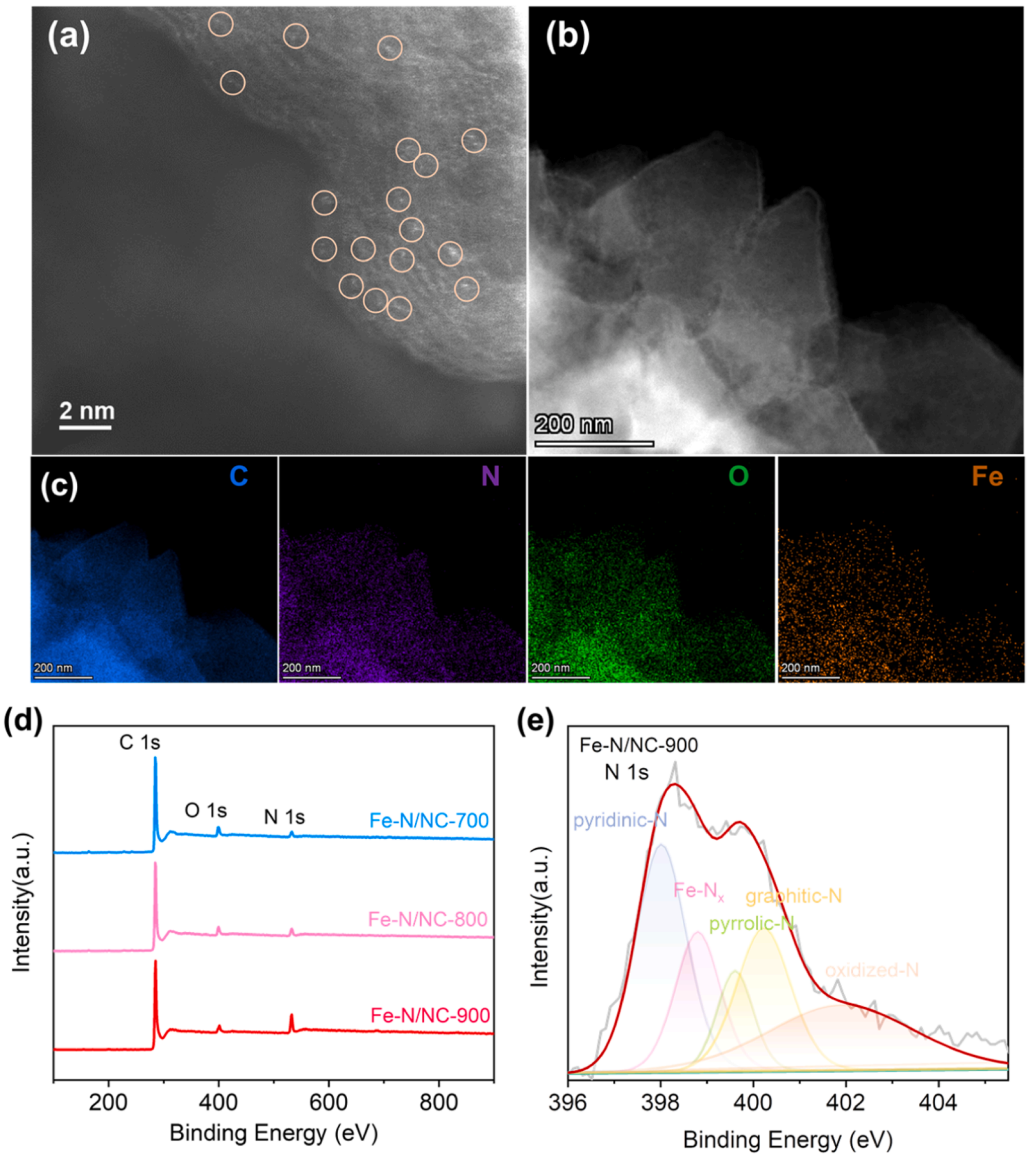

Fig. 3. (a) Atomic-resolution HAADF-STEM image of Fe-N/NC-900. (b) HAADF-STEM images of Fe-N/NC-900, and (c) Elemental mapping images demonstrating the distribution of C (blue), N (purple), O (green), and Fe (orange) elements. (d) XPS survey spectra of Fe-N/NC samples. (e) High-resolution N 1 s spectra of Fe-N/NC-900.

density of nearby C atoms, potentially improving O_2 adsorption and subsequent electrocatalytic ORR at the active sites [39]. Fe–N/NC-900 exhibited the highest combined amounts of pyridinic-N (1.94 at%) and graphitic-N (1.32 at%) among the evaluated samples. Therefore, the high content of Fe–N_x, pyridinic-N and graphitic-N active sites can endow Fe–N/NC-900 with high electrocatalytic activity. Notably, no characteristic peaks associated with Fe were observed in the XPS spectra of the Fe–N/NC samples (Fig. 3d). This absence can be attributed to the dissolution of numerous Fe sites during template removal via acid etching, leaving only a small fraction of firmly anchored Fe sites in the structure. Inductively coupled plasma atomic emission spectrometry revealed similar Fe element contents for Fe–N/NC-700 (0.76%), Fe–N/NC-800 (0.80%) and Fe–N/NC-900 (0.81 wt%) (Fig. S7).

The ORR electrocatalytic performance of the NC-900 and Fe–N/NC samples was initially evaluated using cyclic voltammetry (CV) in an O_2 atmosphere. As shown in Figs. 4a and S8, all samples exhibited distinct ORR peaks, indicating certain ORR electrocatalytic activity. The electrocatalytic activity can be further evaluated by calculating the onset potential (E_{onset}) and half-wave potential ($E_{1/2}$) of the linear sweep voltammetry curves (LSV). As shown in Fig. 4b, the E_{onset} (1.02 V) and $E_{1/2}$ (0.83 V) of Fe–N/NC-900 were comparable to those of 20% Pt/C (E_{onset} = 1.02 V and $E_{1/2}$ = 0.83 V). Furthermore, the E_{onset} and $E_{1/2}$ of Fe–N/NC-900 were more positive than those of NC-900 (E_{onset} = 0.86 V and $E_{1/2}$ = 0.73 V), Fe–N/NC-700 (E_{onset} = 0.98 V and $E_{1/2}$ = 0.78 V) and Fe–N/NC-800 (E_{onset} = 1.02 V and $E_{1/2}$ = 0.81 V). The limiting current density (j_l) of Fe–N/NC-900 reached 6.1 mA cm^{-2}, surpassing that of the 20% Pt/C electrocatalyst (5.70 mA cm^{-2}). The kinetic current density (j_k@0.83 V) of Fe–N/NC-900 was 5.52 mA cm^{-2} similar to that of 20% Pt/C (5.51 mA cm^{-2}) and higher than that of the other samples (Fig. 4c). The Tafel slope of Fe–N/NC-900 was only 88.3 mV dec^{-1} comparable to that of 20% Pt/C (88.7 mV dec^{-1}) and lower than that of the other samples (Fig. 4d). The electrochemically active surface area was determined using double-layer capacitance (C_{dl}) to evaluate the accessible active sites. The C_{dl} was measured by recording CV curves in the potential range of 0.95–1.05 V at various scan rates (Fig. S9). The C_{dl} value for Fe–N/NC-900 was 7.61 mF cm^{-2}, which is markedly higher than that of Fe–N/NC-700 (1.40 mF cm^{-2}) and Fe–N/NC-800 (5.84 mF cm^{-2}), indicating a larger accessible active area for the Fe–N/NC-900

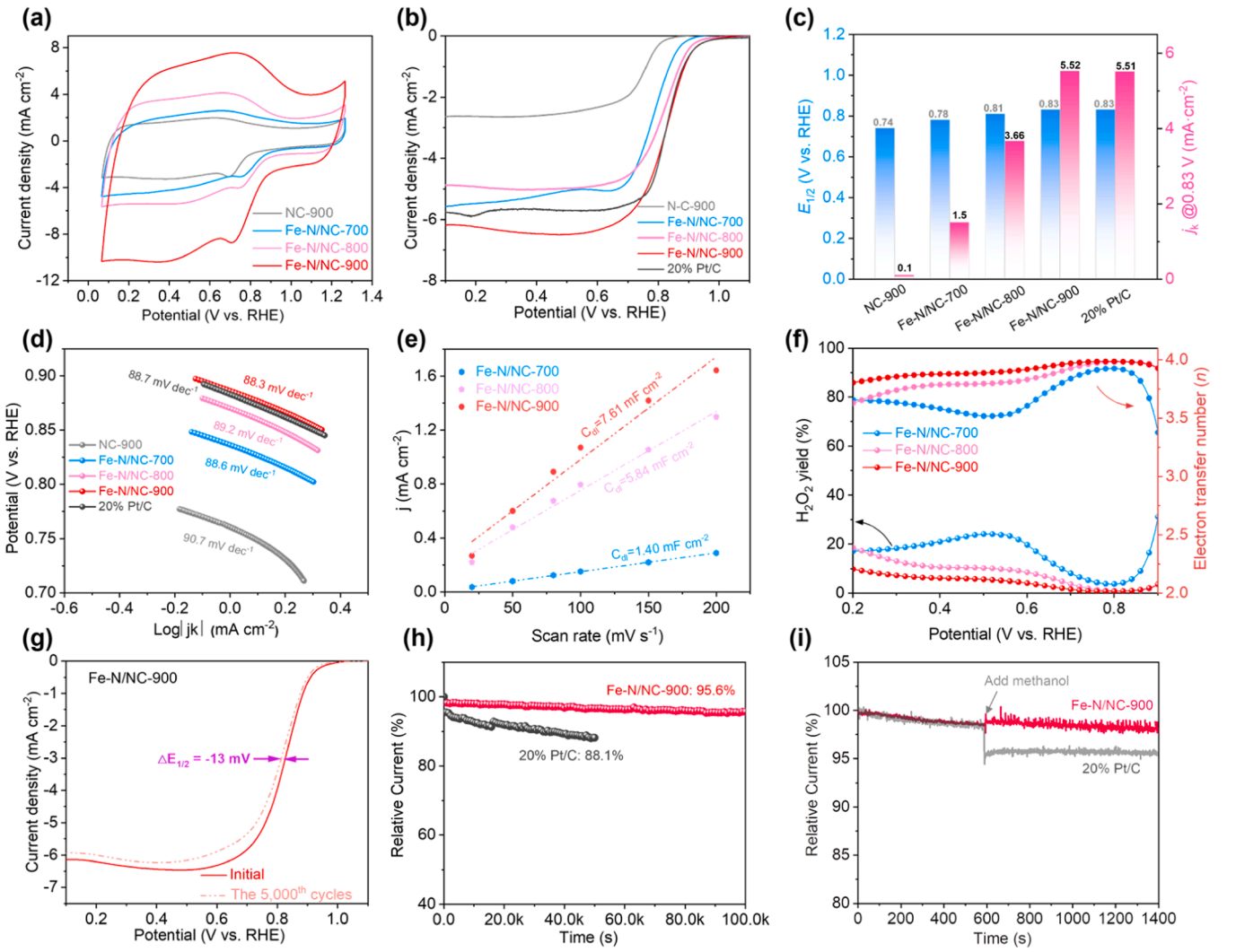

Fig. 4. Electrocatalytic performance evaluation of different catalysts in O_2-saturated 0.1 M KOH solution. (a) CV curve. (b) LVS curves at a rotation rate of 1600 rpm. (c) Comparison of $E_{1/2}$ and j_k at 0.83 V (vs. RHE). (d) Corresponding Tafel plots were obtained from the RDE polarization curves. (e) Electrochemical double-layer capacitance (C_{dl}). (f) H_2O_2 yield and n. (g) The difference of Fe-N/NC-900 before and after the durability test (after 5000 CV cycles). (h) Chronoamperometric measurements of Fe-N/NC-900 and 20% Pt/C at 0.5 V (vs. RHE) with a rotation rate of 1600 rpm. (i) Chronoamperometric measurements of Fe-N/NC-900 and Pt/C catalysts were kept at 0.5 V (vs. RHE) and 1600 rpm with 5.0 mL methanol addition at 600 s.

electrocatalyst during the ORR process (Fig. 4e). Meanwhile, as shown in Table 1, Fe–N/NC-900 exhibited a much higher mass activity (j_m, 2616.06 mA mg_{Fe}^{-1}) and turnover frequency (TOF, 7.71 e^- $site^{-1}$ s^{-1}) at 0.85 V than Fe–N/NC-700 (j_m = 2223.36 mA mg_{Fe}^{-1}, TOF = 6.55 e^- $site^{-1}$ s^{-1}), Fe–N/NC-800 (j_m = 2137.90 mA mg_{Fe}^{-1}, TOF = 6.30 e^- $site^{-1}$ s^{-1}) and 20% Pt/C (j_m = 98.57 mA mg_{Pt}^{-1}, TOF = 1.02 e^- $site^{-1}$ s^{-1}).

The above results indicate that Fe–N/NC-900 exhibits excellent ORR electrocatalytic performance, which can be attributed to the synergistic effect of the atomically dispersed Fe sites, abundant N-containing functional groups (Fe–N_x, pyridinic-N and graphitic-N), high SSA and unique pore structure. Despite the low Fe content, the atomically dispersed Fe sites can considerably enhance the electrocatalytic conversion efficiency. In addition, the high SSA and open micro-/mesoporous structure enhance the exposure of active sites and promote mass transfer and diffusion between the reactants and the electrolyte, thereby improving the overall electrocatalytic performance. Compared with previously reported Fe-based electrocatalysts, Fe–N/NC-900 possesses good ORR activity (Table S4).

Table 1
Comparison of the ORR performance of the prepared electrocatalysts and 20% Pt/C.

Samples	j_m (mA mg_{Fe}^{-1})	TOF (e^- $site^{-1}$ s^{-1})
Fe–N/NC-700	2223.36	6.55
Fe–N/NC-800	2137.90	6.30
Fe–N/NC-900	2616.06	7.71
20% Pt/C	98.57	1.02

Rotating ring–disk electrode measurements were performed on the Fe–N/NC samples to monitor the formation of hydrogen peroxide (H_2O_2) and assess the number of transferred electrons (n), aiming to clarify the ORR electrocatalytic pathways (Fig. S10). Fig. 4f shows that the Fe–N/NC-900 electrocatalyst delivers the lowest H_2O_2 yield (ca. 10%) among the samples, with n ranging from 3.80 to 3.98. This suggests that Fe–N/NC-900 primarily operates via a four-electron process to directly reduce O_2 into H_2O, further confirming its efficient ORR electrocatalytic activity. To verify the role of the Fe–N_x coordination centres as the primary active sites for ORR in the Fe–N/NC-900 electrocatalyst, a poisoning experiment using KSCN was performed. SCN^- ions can strongly coordinate with transition metal centres, blocking O_2 adsorption and consequently suppressing intrinsic ORR activity [40,41]. As shown in Fig. S11, upon adding 10 mM KSCN to the O_2-saturated 0.1 M KOH electrolyte, the ORR performance of Fe–N/NC-900 declined

considerably. The $E_{1/2}$ exhibited a remarkable negative shift of 60 mV, decreasing from 0.83 to 0.77 V, accompanied by a noticeable decrease in the diffusion-limited current density. This pronounced performance degradation, resulting from the masking of metal sites, evidences that the atomically dispersed Fe–N_x moieties are the dominant active centres in the ORR process. Durability is another critical factor for electrocatalysts in practical applications; therefore, accelerated degradation tests were performed to assess the durability of Fe–N/NC-900 and 20% Pt/C. After 5000 and 40,000 cycles in 0.1 M KOH (Fig. 4g and Fig. S12), Fe–N/NC-900 showed a slight decrease in $E_{1/2}$ of 13 and 27 mV, respectively. By contrast, the $E_{1/2}$ of 20% Pt/C decreased by 29 mV after only 5000 CV cycles (Fig. S13). The chronoamperometric response of Fe–N/NC-900 was analysed in an O_2-saturated 0.1 M KOH solution. Fig. 4h shows that the ORR current of Fe–N/NC-900 retained 95.6% of its initial value after 100,000 s, whereas that of 20% Pt/C only retained 88.1% after 50,000 s, demonstrating the superior durability of Fe–N/NC-900 compared with that of 20% Pt/C in an alkaline medium. Furthermore, upon adding 5.0 mL of methanol to the electrolyte, the current density of Fe–N/NC-900 decreased only slightly and rapidly returned to its initial level. By contrast, 20% Pt/C experienced a more pronounced decline in current density and showed limited recovery. This indicates the superior resistance of Fe–N/NC-900 to methanol crossover.

To gain more insight into the intrinsic activity and excellent electrocatalytic performance of Fe–N/NC-900, EIS was conducted. As shown in Fig. S14, the charge transfer resistance (R_{ct}) of Fe–N/NC-900 was 1.11 Ω, slightly lower than that of 20% Pt/C (2.71 Ω). This result indicates that Fe–N/NC-900 exhibits superior charge transfer performance compared with 20% Pt/C, which can be attributed to the high degree of graphitisation in Fe–N/NC-900. This structural feature facilitates electron transfer, thereby enhancing the ORR kinetics. Furthermore, in situ EIS tests, combined with DRT analysis, were performed on Fe–N/NC-700, Fe–N/NC-800 and Fe–N/NC-900 to clarify the mass transport processes [42–44]. Fig. 5a–c shows the results of in situ EIS tests conducted on Fe–N/NC samples in O_2-saturated 0.1 M KOH electrolyte over a continuous potential range of 1.0–0.7. V. For all Fe–N/NC samples, the first semicircle in the high-frequency region (10^5–10^7 Hz) was not affected by the applied potential, as the charge transfer rate at the electrode–solution interface was mainly determined by the intrinsic activity of the electrocatalysts. However, the second semicircle in the low-frequency region (10^{-2}–10^0 Hz) depended on the applied potential. Specifically, the potential range decreased from 1.0 to 0.70 V for Fe–N/NC-700, and the diameter of the second semicircle in the low-frequency region continuously decreased. This suggests that, owing

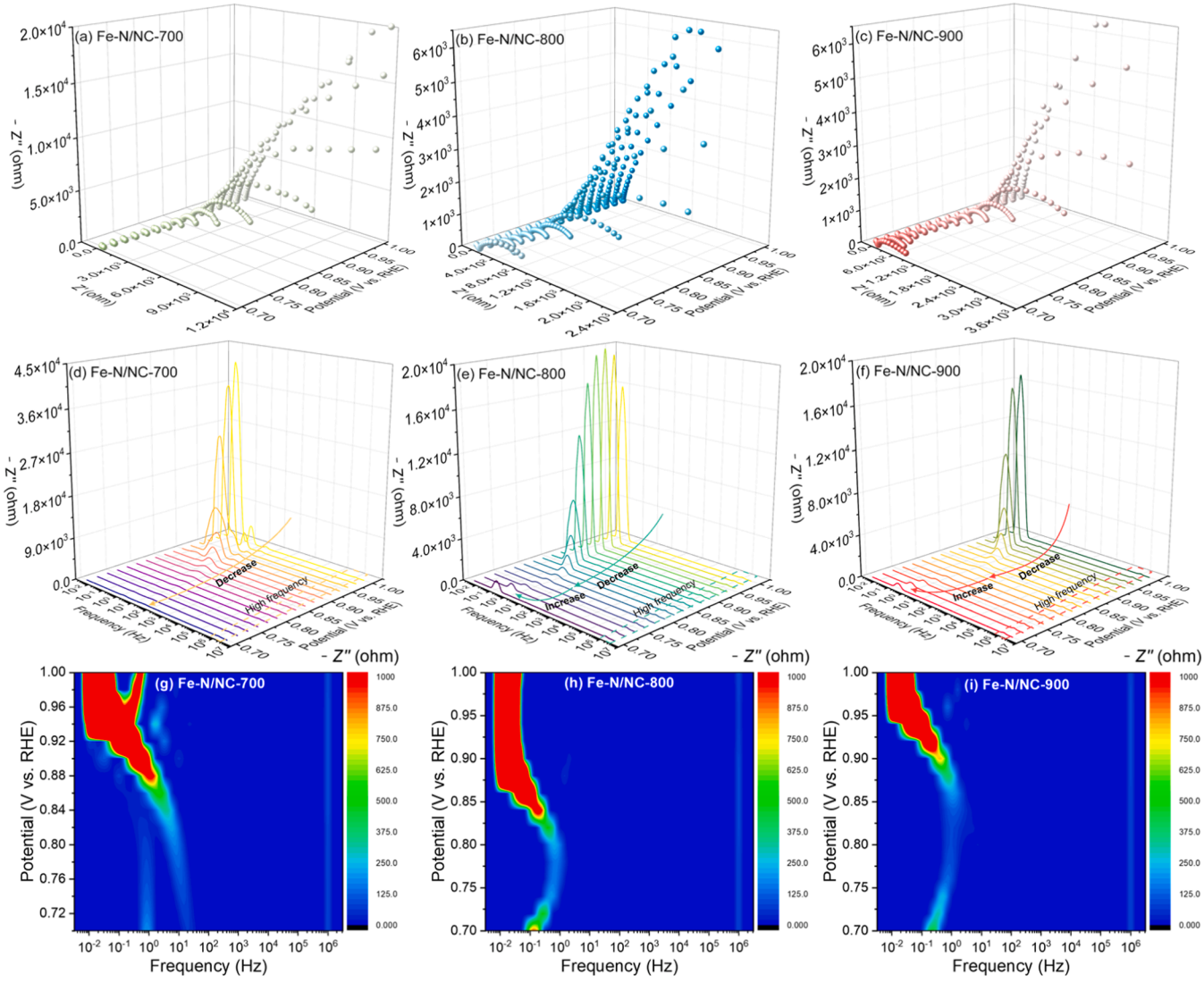

Fig. 5. (a-c) Nyquist plot of in situ EIS measurement, (d-f) in situ DRT analysis, (g-i) two-dimensional contour plot of the in situ DRT for Fe-N/NC-700, Fe-N/NC-800, and Fe-N/NC-900.

to insufficient exposure of active sites and blockage of mass transfer channels in Fe–N/NC-700, the diffusion rate of O_2 to the interface cannot match the charge transfer rate, resulting in a marked kinetic barrier. By contrast, for Fe–N/NC-800 and Fe–N/NC-900, the diameter of the second semicircle in the low-frequency region gradually decreased from 1.0 to 0.80 V and then gradually increased from 0.80 to 0.70 V, indicating that the resistance in the ORR process first decreased and then increased. This phenomenon can be attributed to the high intrinsic activity of the electrocatalysts, resulting in kinetic equilibrium at a critical potential of 0.8. V. Further decreasing the potential led to a sharp decline in the O_2 concentration gradient at the reaction interface, with mass transfer impedance becoming the rate-controlling step. Notably, within the potential range of 0.85–0.75 V, the low-frequency semicircle of Fe–N/NC-900 consistently remained smaller than that of Fe–N/NC-800, corresponding to the mixed control and diffusion control regions, suggesting that Fe–N/NC-900 has lower mass transfer resistance in this region.

The DRT method was further employed to conduct an in-depth analysis of the EIS data. As shown in Fig. 5d–f, the DRT spectra of all samples exhibit two pronounced peaks on the time scale, with the peak intensities corresponding to the resistance during the reaction. The high-frequency region (10^5–10^7 Hz) corresponds to the high-frequency semicircle in the Nyquist plot, and its peak position remains unaltered with applied potential. This can be attributed to the structural stability of the electrocatalysts, which maintains a consistent charge transfer capability throughout the electrochemical process. By contrast, the low-frequency region corresponding to the low-frequency semicircle in the Nyquist plots exhibits remarkable variations in peak position and intensity with potential. Considering the DRT plot of Fe–N/NC-900 (Fig. 5 f) as an example, within the kinetic control range, as the potential decreases from 1.00 to 0.92 V, the low-frequency main peak gradually weakens and shifts towards the high-frequency direction, indicating an acceleration of the reaction kinetics and a reduction in resistance [45, 46]. When the potential further drops to 0.92–0.75 V, the reaction enters the mixed control zone of ORR, with the potential approaching the plateau of the limiting current density and the mass transfer resistance increases accordingly. When the potential reaches 0.70 V, the low-frequency peak considerably strengthens and shifts to lower frequencies, exhibiting typical characteristics of mass transfer control [47, 48]. Fe–N/NC-800 (Fig. 5e) exhibits a similar trend to Fe–N/NC-900, albeit with higher resistance values in each corresponding control zone. Notably, Fe–N/NC-700 (Fig. 5d), constrained by its lower intrinsic electrocatalytic activity, shows sluggish reaction kinetics and no obvious mass transfer control in the DRT analysis. The two-dimensional contour plots of DRT for each sample are presented in Fig. 5g–i. Fe–N/NC-900 transitions more rapidly from the kinetic control regime to the mixed and diffusion control regimes during the ORR process. Moreover, the resistance values associated with each control regime are considerably lower than those of the other samples. These results demonstrate that Fe–N/NC-900 exhibits intrinsically high electrocatalytic activity that accelerates reaction kinetics and its unique open micro-/mesoporous structure facilitates O_2 transport, substantially reducing mass transfer resistance.

The reaction mechanism at the electrocatalytic active sites was thoroughly investigated using density functional theory (DFT) calculations, assuming that the Fe–N_x species in Fe–N/NC-900 primarily exist as Fe–N_4 moieties embedded within the C layer (Fig. 6a). For comparison, a Pt (111) surface was employed as the model for the Pt/C electrocatalyst (Fig. S15). At an applied potential of U = 0 V in an alkaline electrolyte, all elementary steps on the Fe–N_4 and Pt (111) surfaces exhibited a downhill free energy trend (Fig. 6b), indicating that ORR proceeds spontaneously under these conditions.

On the Fe–N_4 site, the OH* desorption step was identified as the rate-determining step, exhibiting a higher thermodynamic barrier (0.62 eV) than on the Pt(111) surface (0.60 eV). As the potential increased to U = 1.23 V (Fig. 6b), the free-energy changes for certain elementary steps became uphill, with the final OH* desorption step being the most endothermic. The theoretical overpotential for this final step on Fe–N/NC-900 was 0.61 V, marginally lower than that of Pt/C (0.63 V). This reduced overpotential indicates the superior OH* desorption capability of Fe–N/NC-900 compared with Pt/C, thereby enhancing the overall ORR kinetics by accelerating the rate-determining removal of OH* intermediates. Furthermore, the open and interconnected micro-/mesoporous structure of the electrocatalyst establishes continuous diffusion pathways. This architecture promotes the transport of species away from the active sites, effectively reducing mass transfer resistance during ORR.

4. Conclusions

A zeolite-assisted strategy was developed to synthesise Fe–N/NC electrocatalysts featuring open micro-/mesoporous structures, atomically dispersed Fe sites and high density of Fe–N_x active centres for ORR. The combination of high SSA and unique pore structures contributes to exposing additional active sites and ensuring efficient mass transfer. Therefore, the optimised Fe–N/NC-900 electrocatalyst demonstrates remarkable ORR performance with a half-wave potential of 0.83 V in alkaline media, excellent selectivity for the four-electron pathway and outstanding long-term durability. Moreover, in situ EIS and DRT analyses demonstrate that the Fe–N/NC-900 electrocatalyst exhibits excellent reaction kinetics and rapid mass transport capability, which can be attributed to its outstanding structural characteristics. DFT analyses reveal that the Fe–N_x sites facilitate desorption of OH* intermediates, thereby promoting ORR. This work proposes a simple and efficient auxiliary strategy for simultaneously constructing atomic-level metal active sites and optimising mass transfer performance, thereby

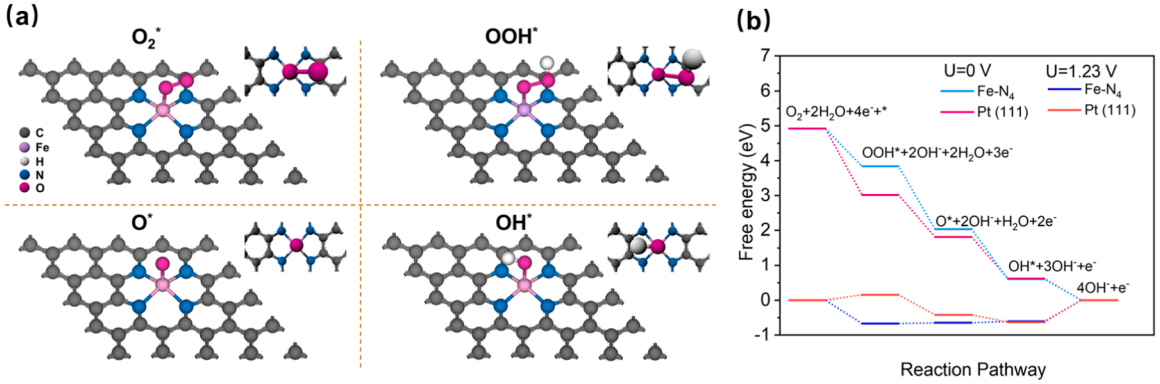

Fig. 6. (a) The stable models of intermediate species adsorbed on Fe-N_4 of Fe-N/NC-900. (b) Free energy ladder diagrams of the reaction pathway in an alkaline environment.

providing a new platform for the innovative design and construction of non-noble-metal ORR electrocatalysts.

CRediT authorship contribution statement

Lin Tao: Supervision, Software. **Chengguo Sun:** Supervision, Software. **Qingdong Li:** Supervision, Software. **Zheyan Tang:** Writing – original draft, Software, Methodology, Formal analysis, Data curation. **Hongwei Zhao:** Writing – review & editing, Resources, Methodology, Data curation. **Xueyuan Zhang:** Supervision, Software. **Baigang An:** Writing – review & editing, Software, Resources, Methodology, Formal analysis, Data curation. **Meiyu Chen:** Resources, Formal analysis, Data curation. **Lixiang Li:** Writing – review & editing, Supervision, Resources, Methodology, Data curation. **Siqi Guan:** Supervision, Methodology. **Lin Wu:** Methodology, Data curation. **Huaiyang Zuo:** Methodology. **Han Zhang:** Supervision, Methodology. **Jingang Zheng:** Supervision, Formal analysis.

Declaration of Competing Interest

The authors declare that they have no known competing financial interests or personal relationships that could have appeared to influence the work reported in this paper.

Acknowledgements

We acknowledge the financial support by grants from the National Natural Science Foundation of China (51872131, 52371224, 52304330), the Startup Fund for Doctoral Research of Liaoning (2023-BS-184), the University of Science and Technology Liaoning Talent Project Grants (6003000315), and the Fundamental Research Funds for the Liaoning Universities (LJ222410146062, LJ212410146075). The authors extend their gratitude to Ms. Larissa King from Scientific Compass (www.shiyanjia.com) for the language editing service.

Appendix A. Supporting information

Supplementary data associated with this article can be found in the online version at doi:10.1016/j.jallcom.2026.188545.

References

[1] X. Tian, X. Zhao, Y.Q. Su, L. Wang, H. Wang, D. Dang, B. Chi, H. Liu, E.J. M. Hensen, X.W. Lou, B.Y. Xia, Engineering bunched Pt-Ni alloy nanocages for efficient oxygen reduction in practical fuel cells, Science 366 (2019) 850–856.
[2] M. Luo, Z. Zhao, Y. Zhang, Y. Sun, Y. Xing, F. Lv, Y. Yang, X. Zhang, S. Hwang, Y. Qin, J.-Y. Ma, F. Lin, D. Su, G. Lu, S. Guo, PdMo bimetallene for oxygen reduction catalysis, Nature 574 (2019) 81–85.
[3] M. Escudero-Escribano, P. Malacrida, M.H. Hansen, U.G. Vej-Hansen, A. Velázquez-Palenzuela, V. Tripkovic, J. Schiøtz, J. Rossmeisl, I.E.L. Stephens, I. Chorkendorff, Tuning the activity of Pt alloy electrocatalysts by means of the lanthanide contraction, Science 352 (2016) 73–76.
[4] J. Cui, D. Zhang, Z. Liu, C. Li, T. Zhang, S. Yin, Y. Song, H. Li, H. Li, C. Li, Carbon-anchoring synthesis of Pt1Ni1@Pt/C core-shell catalysts for stable oxygen reduction reaction, Nat. Commun. 15 (2024) 9458.
[5] A.A. Alekseenko, K.O. Paperzh, A.S. Pavlets, S.V. Belenov, E.A. Moguchikh, A. K. Nevelskaya, Y.A. Bayan, M.V. Danilenko, I.V. Pankov, V.E. Guterman, Enhanced Pt/C and PtCu/C electrocatalysts for improved oxygen reduction reaction in proton-exchange membrane fuel cells, J. Mater. Sci. 60 (2025) 5035–5051.
[6] R. Kumar, M. Mooste, Z. Ahmed, S. Akula, I. Zekker, M. Marandi, M. Käärik, J. Leis, A. Kikas, A. Treshchalov, M. Otsus, J. Aruväli, V. Kisand, A. Tamm, K. Tammeveski, Highly active ZIF-8@CNT composite catalysts as cathode materials for anion exchange membrane fuel cells, Ind. Chem. Mater. 1 (2023) 526–541.
[7] D. Geng, Y. Huang, S. Yuan, Y. Jiang, H. Ren, S. Zhang, Z. Liu, J. Feng, T. Wei, Z. Fan, Coordination engineering of defective cobalt–nitrogen–carbon electrocatalysts with graphene quantum dots for boosting oxygen reduction reaction, Small 19 (2023) 2207227.
[8] Y. Li, M.Y. Chen, B.A. Lu, H.R. Wu, J.N. Zhang, Unravelling the role of hydrogen peroxide in pH-dependent ORR performance of Mn-N-C catalysts, Appl. Catal. B-Environ. 342 (2024) 123458.
[9] Q. Shi, Q. Zhu, Y. Hou, Y. Wang, C. Zhang, C. Wu, Y. Hao, Co-NC foam for peroxymonosulfate activation: highly sp2/sp3 hybrid carbon enhances electron transfer capacity, Chem. Eng. J. 516 (2025) 164180.
[10] R. Kumar, M. Mooste, I. Zekker, M. Käärik, J. Leis, A. Kikas, A. Treshchalov, J. Kozlova, M. Otsus, J. Aruväli, V. Kisand, K. Kukli, K. Tammeveski, Tailoring highly efficient ZIF-derived FexCey@N–C composite catalysts for oxygen reduction reaction in H-shape microbial fuel cells, Int. J. Hydrog. Energy 98 (2025) 793–806.
[11] Z. Tang, H. Zhao, L. Tao, W. Liu, L. Li, Y. Shi, J. Zheng, L. Wu, H. Zhang, F. Di, C. Sun, Z. Yao, Y. Qin, B. An, Iron-embedded hollow-out nitrogen-doped carbon nanoboxes catalyst with enhanced oxygen transport for improved ORR performance, Int. J. Hydrog. Energy 228 (2026) 154698.
[12] K. Liu, J. Fu, Y. Lin, T. Luo, G. Ni, H. Li, Z. Lin, M. Liu, Insights into the activity of single-atom Fe-N-C catalysts for oxygen reduction reaction, Nat. Commun. 13 (2022) 2075.
[13] Y. Ni, W. Xie, J. Chen, Revealing insights into the axial coordination effect of M–N4 catalysts on electrocatalytic activity towards the oxygen reduction reaction, J. Mater. Chem. A 11 (2023) 23080–23086.
[14] Y.J. Sa, D.J. Seo, J. Woo, J.T. Lim, J.Y. Cheon, S.Y. Yang, J.M. Lee, D. Kang, T. J. Shin, H.S. Shin, H.Y. Jeong, C.S. Kim, M.G. Kim, T.Y. Kim, S.H. Joo, A general approach to preferential formation of active Fe–Nx Sites in Fe–N/C electrocatalysts for efficient oxygen reduction reaction, J. Am. Chem. Soc. 138 (2016) 15046–15056.
[15] J. Wei, D. Xia, Y. Wei, X. Zhu, J. Li, L. Gan, Probing the oxygen reduction reaction intermediates and dynamic active site structures of molecular and pyrolyzed Fe–N–C electrocatalysts by in situ Raman spectroscopy, ACS Catal. 12 (2022) 7811–7820.
[16] M. Liu, H. Su, X. Liu, X. He, P. Tan, F. Liu, J. Pan, Dynamic modulation of electron redistribution at the heterogeneous interface nickel hydroxides/platinum boosts acidic oxygen reduction reaction, Nat. Commun. 16 (2025) 2826.
[17] H. Zhao, Y. Zhang, L. Li, X. Geng, H. Yang, W. Zhou, C. Sun, B. An, Synthesis of an ordered porous carbon with the dual nitrogen-doped interfaces and its ORR catalysis performance, Chin. Chem. Lett. 32 (2021) 140–145.
[18] Y. Zhan, Z.B. Ding, F. He, X. Lv, W.F. Wu, B. Lei, Y. Liu, X.B. Yan, Active site switching of Fe-N-C as a chloride-poisoning resistant catalyst for efficient oxygen reduction in seawater-based electrolyte, Chem. Eng. J. 443 (2022) 136456.
[19] S. Yin, H. Yi, M. Liu, J. Yang, S. Yang, B.-W. Zhang, L. Chen, X. Cheng, H. Huang, R. Huang, Y. Jiang, H. Liao, S. Sun, An in situ exploration of how Fe/N/C oxygen reduction catalysts evolve during synthesis under pyrolytic conditions, Nat. Commun. 15 (2024) 6229.
[20] S. Zhao, J. Li, R. Wang, J. Cai, S. Zang, Electronically and geometrically modified single-atom Fe sites by adjacent fe nanoparticles for enhanced oxygen reduction, Adv. Mater. 34 (2022) e2107291.
[21] J. Ma, J. Li, R. Wang, Y. Yang, P. Yin, J. Mao, T. Ling, S. Qiao, Hierarchical porous S-doped Fe–N–C electrocatalyst for high-power-density zinc–air battery, Mater. Today Energy 19 (2021) 100624.
[22] J. Zhu, A. Pedersen, S. Kellner, R.D. Hunter, J. Barrio, Impact of ionomers on porous Fe-N-C catalysts for alkaline oxygen reduction in gas diffusion electrodes, Commun. Chem. 8 (2025) 27.
[23] M. Kim, K.L. Firestein, J.F.S. Fernando, X. Xu, H. Lim, D.V. Golberg, J. Na, J. Kim, H. Nara, J. Tang, Y. Yamauchi, Strategic design of Fe and N co-doped hierarchically porous carbon as superior ORR catalyst: from the perspective of nanoarchitectonics, Chem. Sci. 13 (2022) 10836–10845.
[24] J. Han, H. Bao, J. Wang, L. Zheng, S. Sun, Z. Wang, C. Sun, 3D N-doped ordered mesoporous carbon supported single-atom Fe-N-C catalysts with superior performance for oxygen reduction reaction and zinc-air battery, Appl. Catal. B-Environ. 280 (2021) 119411.
[25] T. Zhu, W. Lyu, Y. Wang, X. Mi, Y. Liao, Hierarchical meso-micro porous FeNC derived from tripolycyanamide-based microporous polymer as efficient electrocatalyst for oxygen reduction reaction, J. Colloid Interface Sci. 633 (2023) 265–274.
[26] H. Xu, D. Wang, P. Yang, L. Du, X. Lu, R. Li, L. Liu, J. Zhang, M. An, A hierarchically porous Fe-N-C synthesized by dual melt-salt-mediated template as advanced electrocatalyst for efficient oxygen reduction in zinc-air battery, Appl. Catal. B-Environ. 305 (2022) 121040.
[27] H. Zhao, L. Li, Y. Liu, X. Geng, H. Yang, C. Sun, B. An, Synthesis and ORR performance of nitrogen-doped ordered microporous carbon by CVD of acetonitrile vapor using silanized zeolite as template, Appl. Surf. Sci. 504 (2020) 144438.
[28] K.D. Mondale, R.M. Carland, F.F. Aplan, The comparative ion exchange capacities of natural sedimentary and synthetic zeolites, Miner. Eng. 8 (1995) 535–548.
[29] W. Li, G. Wu, W. Hu, J. Dang, C. Wang, X. Weng, I. da Silva, P. Manuel, S. Yang, N. Guan, L. Li, Direct Propylene Epoxidation with Molecular Oxygen over Cobalt-Containing Zeolites, J. Am. Chem. Soc. 144 (2022) 4260–4268.
[30] H. Zhao, L. Li, H. Zuo, D. Qu, H. Zhang, L. Tao, C. Sun, D. Ju, B. An, Large-scale synthesis of 3D ordered microporous carbon at low temperature using cobalt ions exchanged zeolite Y as a template, N. Carbon Mater. 38 (2023) 861–874.
[31] G. Moon, A. Bähr, H. Tüysüz, Structural Engineering of 3D Carbon Materials from Transition Metal Ion-Exchanged Y Zeolite Templates, Chem. Mater. 30 (2018) 3779–3788.
[32] K. Niu, G. Li, J. Liu, Y. Wei, One step synthesis of Fe-SSZ-13 zeolite by hydrothermal method, J. Solid State Chem. 287 (2020) 121330.
[33] L. Bieseki, A. Habrioux, J. Paillaud, S. Pergher, J. Rousseau, I. Batonneau-Gener, E. Oheix, A. Sachse, A zeolite-templated carbon synthesized from extralarge-pore zeolite ZEO-1, Inorg. Chem. 63 (2024) 19509–19512.
[34] H. Nishihara, T. Kyotani, Zeolite-templated carbons – three-dimensional microporous graphene frameworks, Chem. Commun. 54 (2018) 5648–5673.
[35] K. Xuan, Y. Liu, X. Zhu, Y. Xiao, L. Zhong, R.M. Othman, G.P. Lithoxoos, F. Almansour, A.N. Shakhs, X. Sun, W.-P. Pan, Pelletizing zeolite templated carbon for carbon capture: developing an analytics-driven framework for binder selection, Sep. Purif. Technol. 374 (2025) 133694.

[36] L. Wu, S. Li, L. Li, H. Zhang, L. Tao, X. Geng, H. Yang, W. Zhou, C. Sun, D. Ju, B. An, Modest modulation on the electronic structure of Co9S8 by vanadium doping for high-performance rechargeable Zn–air batteries, Appl. Catal. B-Environ. 324 (2023) 122250.
[37] R.S. Ribeiro, A.L.S. Vieira, K. Biernacki, A.L. Magalhães, J.J. Delgado, R.G. Morais, N. Rey-Raap, R.P. Rocha, M.F.R. Pereira, Engineering single-atom Fe–N active sites on hollow carbon spheres for oxygen reduction reaction, Carbon 213 (2023) 118192.
[38] Y. Wang, Q. Li, L. Zhang, Y. Wu, H. Chen, T. Li, M. Xu, S. Bao, A gel-limiting strategy for large-scale fabrication of Fe–N–C single-atom ORR catalysts, J. Mater. Chem. A 9 (2021) 7137–7142.
[39] G. Xing, G. Zhang, B. Wang, M. Tong, C. Tian, L. Wang, H. Fu, Strengthening oxygen reduction activity based on the cooperation of pyridinic-N and graphitic-N for atomically dispersed Fe sites, J. Mater. Chem. A 11 (2023) 9493–9503.
[40] M.S. Thorum, J.M. Hankett, A.A. Gewirth, Poisoning the oxygen reduction reaction on carbon-supported Fe and Cu electrocatalysts: evidence for metal-centered activity, J. Phys. Chem. Lett. 2 (2011) 295–298.
[41] X. Liang, Z. Li, H. Xiao, T. Zhang, P. Xu, H. Zhang, Q. Gao, L. Zheng, Two types of single-atom FeN4 and FeN5 electrocatalytic active centers on n-doped carbon driving high performance of the SA-Fe-NC oxygen reduction reaction catalyst, Chem. Mater. 33 (2021) 5542–5554.
[42] J. Huang, N.P. Sullivan, A. Zakutayev, R. O'Hayre, How reliable is distribution of relaxation times (DRT) analysis? A dual regression-classification perspective on DRT estimation, interpretation, and accuracy, Electrochim. Acta 443 (2023) 141879.
[43] C. Jia, Y. Zhao, S. Song, Q. Sun, Q. Meyer, S. Liu, Y. Shen, C. Zhao, Highly ordered hierarchical porous single-atom Fe catalyst with promoted mass transfer for efficient electroreduction of CO2, Adv. Energy Mater. 13 (2023) 2302007.
[44] J. Wu, Y. Zhu, A. Cai, X. Fan, W. Peng, Y. Li, Structural engineering of Fe single-atom oxygen reduction catalyst with high site density and improved mass transfer, J. Energy Chem. 98 (2024) 634–644.
[45] S. Liu, Q. Meyer, C. Jia, S. Wang, C. Rong, Y. Nie, C. Zhao, Operando deconvolution of the degradation mechanisms of iron–nitrogen–carbon catalysts in proton exchange membrane fuel cells, Energy Environ. Sci. 16 (2023) 3792–3802.
[46] M. Heinzmann, A. Weber, E. Ivers-Tiffée, Advanced impedance study of polymer electrolyte membrane single cells by means of distribution of relaxation times, J. Power Sources 402 (2018) 24–33.
[47] Q. Meyer, S. Liu, Y. Li, C. Zhao, Operando detection of oxygen reduction reaction kinetics of Fe–N–C catalysts in proton exchange membrane fuel cells, J. Power Sources 533 (2022) 231058.
[48] A. Weiß, S. Schindler, S. Galbiati, M.A. Danzer, R. Zeis, Distribution of relaxation times analysis of high-temperature PEM fuel cell impedance spectra, Electrochim. Acta 230 (2017) 391–398.